

Supplementary Materials: Emergence of tunable intersubband-plasmon-polaritons in graphene superlattices

Minwoo Jung^{1,*} and Gennady Shvets^{2,†}

¹*Department of Physics, Cornell University, Ithaca, New York, 14853, USA*

²*School of Applied and Engineering Physics, Cornell University, Ithaca, New York 14853, USA*

(Dated: January 24, 2023)

I. BOUND STATES OF DIRAC ELECTRONS IN SQUARE POTENTIAL WELLS

Here, we provide an analytical solution for bound states based on total internal reflection of electrons with Dirac dispersion (TIREDD) in a square potential well or a square potential barrier. Suppose a square potential well ($U_0 < U_1$) or a square potential barrier ($U_0 > U_1$) given as

$$U_E(x) = U_0 \quad (0 < x < W), \quad U_1 \quad (\text{elsewhere}). \quad (\text{S1})$$

Then, we can set an ansatz for a bound state with eigenenergy E as

$$\psi(\mathbf{r}) = e^{ik_y y} \times \begin{cases} L \begin{bmatrix} 1 \\ \frac{-i\alpha + ik_y}{(E-U_1)/\hbar v_F} \end{bmatrix} e^{\alpha x} & (x < 0) \\ A \begin{bmatrix} 1 \\ \frac{q + ik_y}{(E-U_0)/\hbar v_F} \end{bmatrix} e^{iqx} + B \begin{bmatrix} 1 \\ \frac{-q + ik_y}{(E-U_0)/\hbar v_F} \end{bmatrix} e^{-iqx} & (0 < x < W), \\ R \begin{bmatrix} 1 \\ \frac{i\alpha + ik_y}{(E-U_1)/\hbar v_F} \end{bmatrix} e^{-\alpha x} & (x > W) \end{cases}, \quad (\text{S2})$$

where $q = \sqrt{\left(\frac{E-U_0}{\hbar v_F}\right)^2 - k_y^2}$ is the momentum along x -axis within the well/barrier, and $\alpha = \sqrt{k_y^2 - \left(\frac{E-U_1}{\hbar v_F}\right)^2}$ is the decaying factor outside the well/barrier. Both q and α are real; therefore, this ansatz is possible only when $|E - U_1| < \hbar v_F k_y < |E - U_0|$.

By imposing the continuity of ψ and the continuity of probability current $\mathbf{J} = \psi^\dagger \sigma_x \psi \hat{\mathbf{x}} + \psi^\dagger \sigma_y \psi \hat{\mathbf{y}}$, we obtain the following condition for the eigenenergy E :

$$\tan(qW) = \frac{q\alpha}{\frac{E-U_0}{\hbar v_F} \frac{E-U_1}{\hbar v_F} - k_y^2}. \quad (\text{S3})$$

Figure S1a shows the inverse tangent of the right hand side of the above equation. Since the right hand side is vanishing in most region, the bound state energy condition simply reduces to $\tan(qW) \sim 0$. Therefore, we get $E_j \sim \hbar v_F \sqrt{(\pi j/W)^2 + k_y^2} + U_0$, which we discussed in the main text. Figure S1b shows that a potential barrier also can host bound states via TIREDD of the valence band electrons, as discussed in the main text.

II. NUMERICAL METHOD FOR THE CALCULATION OF HIPP DISPERSION AND NORMAL REFLECTION SPECTRUM

In this section, we elaborate on the numerical method used for the calculation of HIPP dispersion and normal reflection spectrum shown in the main text. As discussed in the main text, we only consider the transverse magnetic modes that can be described with E_x , E_z and B_y . Also, we consider the dispersion in the momentum along x -axis ($\mathbf{q} = q\hat{\mathbf{x}}$).

Recall that the metagate periodicity is L , and the width of air gaps in the metagate is S . For convenience, let's define several variables to describe the plane wave solutions in each of the layers—the air above all layers (A), hBN layers

* mj397@cornell.edu

† gs656@cornell.edu

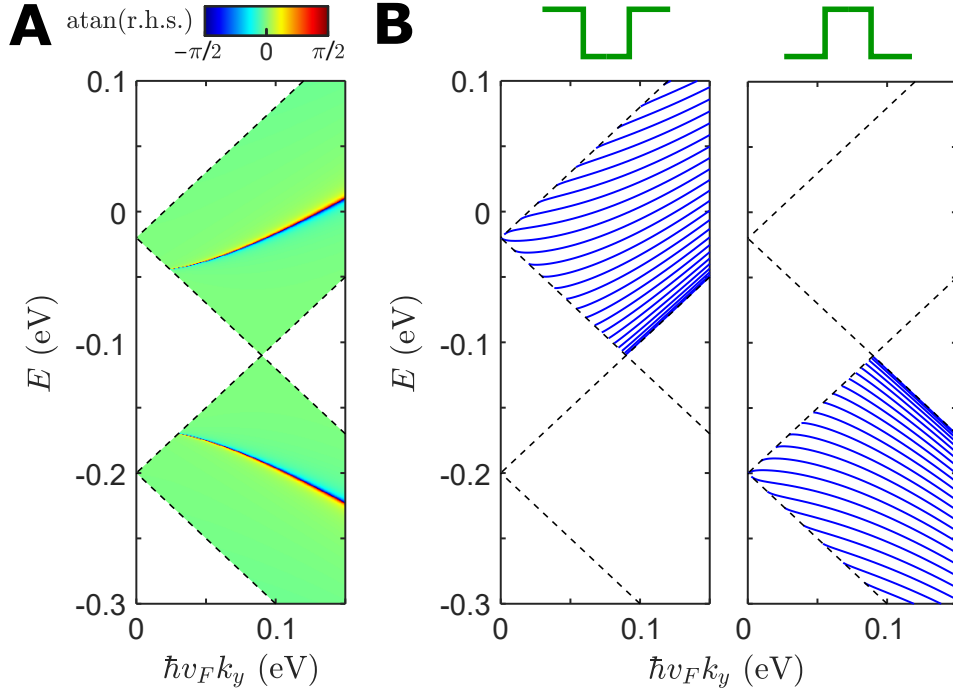


FIG. S1. **a.** Plotting the inverse tangent of the right hand side of Eq. (S3); $U_0 = -0.2\text{eV}$, $U_1 = -0.02\text{eV}$ (or $U_0 = -0.02\text{eV}$, $U_1 = -0.2\text{eV}$; both yield the same result), and $W = 200\text{nm}$ ($v_F = 1.1 \times 10^6\text{m/s}$). **b.** Dispersion of bound states in k_y for a potential well (left: $U_0 = -0.2\text{eV}$, $U_1 = -0.02\text{eV}$) and for a potential barrier (left: $U_0 = -0.02\text{eV}$, $U_1 = -0.2\text{eV}$). The dashed lines refer to $\hbar v_F k_y = |E - U_0|$ and $\hbar v_F k_y = |E - U_1|$.

(B), the oxide layer (O), and the substrate (S): $q_m = q + \frac{2\pi m}{L}$, $q_\omega = \frac{\omega}{c}$, $\kappa_m^A = -i\sqrt{q_\omega^2 - q_m^2}$, $\kappa_m^B = -i\sqrt{\epsilon_{xy}^B q_\omega^2 - \frac{\epsilon_z^B}{\epsilon_z} q_m^2}$, $\kappa_m^O = -i\sqrt{\epsilon^O q_\omega^2 - q_m^2}$, and $\kappa_m^S = -i\sqrt{\epsilon^S q_\omega^2 - q_m^2}$, where $m \in \mathbb{Z}$ is an integer index. To describe the modes (E_x , E_z and B_y) in the air gaps of the metagate (M): $\eta_\mu = \frac{\pi\mu}{S}$, $\phi_\mu(x) = \sqrt{2 - \delta_{\mu 0}} \cos[\eta_\mu(x - \frac{L-S}{2})]$, and $\kappa_\mu^M = -i\sqrt{q_\omega^2 - \eta_\mu^2}$, where μ is a non-negative integer index.

Then, we can set an ansatz for the HIPP mode as below.

(i) In the air above the top hBN layer ($z > h_t$):

$$\begin{aligned}
 cB_y &= \sum_m e^{iq_m x} \left(R_m e^{-\kappa_m^A(z-h_t)} + I_m e^{\kappa_m^A(z-h_t)} \right) \\
 k_\omega E_x &= -i \sum_m e^{iq_m x} \kappa_m^A \left(-R_m e^{-\kappa_m^A(z-h_t)} + I_m e^{\kappa_m^A(z-h_t)} \right) \\
 k_\omega E_z &= - \sum_m e^{iq_m x} q_m \left(R_m e^{-\kappa_m^A(z-h_t)} + I_m e^{\kappa_m^A(z-h_t)} \right).
 \end{aligned} \tag{S4}$$

Here, R_0 is the reflection coefficient, in the presence of the normal ($q = 0$) incident light $I_m = \delta_{m0}$. An eigenmode exists even with vanishing external drive term $I_m = 0$.

(ii) In the top hBN layer ($0 < z < h_t$):

$$\begin{aligned}
 cB_y &= \sum_m e^{iq_m x} \left(A_m \cosh(\kappa_m^B z) + B_m \sinh(\kappa_m^B z) \right) \\
 k_\omega E_x &= \frac{-i}{\epsilon_{xy}^B} \sum_m e^{iq_m x} \kappa_m^B \left(A_m \sinh(\kappa_m^B z) + B_m \cosh(\kappa_m^B z) \right) \\
 k_\omega E_z &= \frac{-1}{\epsilon_z^B} \sum_m e^{iq_m x} q_m \left(A_m \cosh(\kappa_m^B z) + B_m \sinh(\kappa_m^B z) \right)
 \end{aligned} \tag{S5}$$

(iii) In the bottom hBN layer ($-h_b < z < 0$):

$$\begin{aligned}
cB_y &= \sum_m e^{iq_m x} (C_m \cosh(\kappa_m^B z) + B_m \sinh(\kappa_m^B z)) \\
k_\omega E_x &= \frac{-i}{\epsilon_{xy}^B} \sum_m e^{iq_m x} \kappa_m^B (C_m \sinh(\kappa_m^B z) + B_m \cosh(\kappa_m^B z)) \\
k_\omega E_z &= \frac{-1}{\epsilon_z^B} \sum_m e^{iq_m x} q_m (C_m \cosh(\kappa_m^B z) + B_m \sinh(\kappa_m^B z))
\end{aligned} \tag{S6}$$

(iv) In the air gap of the metagate ($-h_b - h_m < z < -h_b$):

$$\begin{aligned}
cB_y &= \sum_\mu \phi_\mu(x) (D_\mu \cosh(\kappa_\mu^M(z + h_b)) + E_\mu \sinh(\kappa_\mu^M(z + h_b))) \\
k_\omega E_x &= -i \sum_\mu \phi_\mu(x) \kappa_\mu^M (D_\mu \sinh(\kappa_\mu^M(z + h_b)) + E_\mu \cosh(\kappa_\mu^M(z + h_b))) \\
k_\omega E_z &= i \sum_\mu \partial_x \phi_\mu(x) (D_\mu \cosh(\kappa_\mu^M(z + h_b)) + E_\mu \sinh(\kappa_\mu^M(z + h_b)))
\end{aligned} \tag{S7}$$

(v) In the oxide layer ($-h_b - h_m - h_o < z < -h_b - h_m$):

$$\begin{aligned}
cB_y &= \sum_m e^{iq_m x} (F_m \cosh(\kappa_m^O(z + h_b + h_m)) + G_m \sinh(\kappa_m^O(z + h_b + h_m))) \\
k_\omega E_x &= \frac{-i}{\epsilon^O} \sum_m e^{iq_m x} \kappa_m^O (F_m \sinh(\kappa_m^O(z + h_b + h_m)) + G_m \cosh(\kappa_m^O(z + h_b + h_m))) \\
k_\omega E_z &= \frac{-1}{\epsilon^O} \sum_m e^{iq_m x} q_m (F_m \cosh(\kappa_m^O(z + h_b + h_m)) + G_m \sinh(\kappa_m^O(z + h_b + h_m)))
\end{aligned} \tag{S8}$$

(vi) In the substrate ($z < -h_b - h_m - h_o$):

$$\begin{aligned}
cB_y &= \sum_m e^{iq_m x} H_m e^{\kappa_m^S(z + h_b + h_m + h_o)} \\
k_\omega E_x &= \frac{-i}{\epsilon^S} \sum_m e^{iq_m x} \kappa_m^S H_m e^{\kappa_m^S(z + h_b + h_m + h_o)} \\
k_\omega E_z &= \frac{-1}{\epsilon^S} \sum_m e^{iq_m x} q_m H_m e^{\kappa_m^S(z + h_b + h_m + h_o)}
\end{aligned} \tag{S9}$$

At $z = 0$, we can define the dynamic electric potential field on graphene δU_E from $-\partial_x(\delta U_E/(-e)) = E_x(z = 0)$, and the dynamic carrier density oscillation δn from $-e\delta n = D_z(z = 0^+) - D_z(z = 0^-)$

$$\begin{aligned}
k_\omega \delta U_E &= \frac{-e}{\epsilon_{xy}^B} \sum_m \frac{\kappa_m^B}{q_m} B_m e^{iq_m x} \\
k_\omega \delta n &= \frac{1}{e} \sum_m q_m (A_m - C_m) e^{iq_m x}
\end{aligned} \tag{S10}$$

Now, we match the boundary conditions (continuity of E_x and continuity of B_y with no free current density). At $z = 0$, due to the current density at graphene, we get $B_y(z = 0^+) - B_y(z = 0^-) = -\mu_0 \sigma * E_x(z = 0)$. Again, for convenience, let's define several vector/matrix notations:

$$\begin{aligned}
\{A_m\}, \{B_m\}, \dots, \{I_m\}, \{R_m\} &\rightarrow A, B, \dots, I, R, \\
[\mathcal{C}_t]_{mm'} &= \delta_{mm'} \cosh(\kappa_m^B h_t), [\mathcal{S}_t]_{mm'} = \delta_{mm'} \sinh(\kappa_m^B h_t), \\
[\mathcal{C}_b]_{mm'} &= \delta_{mm'} \cosh(\kappa_m^B h_b), [\mathcal{S}_b]_{mm'} = \delta_{mm'} \sinh(\kappa_m^B h_b), \\
[\mathcal{C}_m]_{\mu\mu'} &= \delta_{\mu\mu'} \cosh(\kappa_\mu^M h_m), [\mathcal{S}_m]_{\mu\mu'} = \delta_{\mu\mu'} \sinh(\kappa_\mu^M h_m), \\
[\mathcal{C}_o]_{mm'} &= \delta_{mm'} \cosh(\kappa_m^O h_o), [\mathcal{S}_o]_{mm'} = \delta_{mm'} \sinh(\kappa_m^O h_o), \\
[\mathcal{K}^A]_{mm'} &= \delta_{mm'} \kappa_m^A, [\mathcal{K}^B]_{mm'} = \delta_{mm'} \kappa_m^B / \epsilon_{xy}^B, [\mathcal{K}^M]_{\mu\mu'} = \delta_{\mu\mu'} \kappa_\mu^M, [\mathcal{K}^O]_{mm'} = \delta_{mm'} \kappa_m^O / \epsilon^O, [\mathcal{K}^S]_{mm'} = \delta_{mm'} \kappa_m^S / \epsilon^S, \\
[\mathcal{Q}]_{mm'} &= \delta_{mm'} q_m,
\end{aligned}$$

$[\Sigma]_{mm'} = -i\sigma(q_n, q_m, \omega)$, and $[\mathcal{T}]_{\mu m} = \frac{1}{S} \int_S dx \psi_\mu^*(x) e^{iq_m x}$. Here, \mathcal{T} is the basis transformation matrix (from plane waves to the eigenmodes in the air gap). From the boundary conditions, we get:

(i) Between the air and the top hBN:

$$\begin{aligned} \mathcal{C}_t A + \mathcal{S}_t B &= R + I \\ \mathcal{K}^B (\mathcal{S}_t A + \mathcal{C}_t B) &= \mathcal{K}^A (-R + I) \end{aligned} \quad (\text{S11})$$

(ii) Between the top and the bottom hBN:

$$C - A = \frac{1}{\omega} \Sigma \mathcal{K}^B B \quad (\text{S12})$$

(iii) Between the bottom BN and the air gap of the metagate:

$$\begin{aligned} D &= \mathcal{T} (\mathcal{C}_b C - \mathcal{S}_b B) \\ \mathcal{K}^M E &= \mathcal{T} \mathcal{K}^B (\mathcal{C}_b B - \mathcal{S}_b C) \\ \frac{S}{L} \mathcal{T}^\dagger \mathcal{K}^M E &= \mathcal{K}^B (\mathcal{C}_b B - \mathcal{S}_b C) \end{aligned} \quad (\text{S13})$$

(iv) Between the air gap of the metagate and the oxide:

$$\begin{aligned} \mathcal{C}_m D - \mathcal{S}_m E &= \mathcal{T} F \\ \mathcal{K}^M (\mathcal{C}_m E - \mathcal{S}_m D) &= \mathcal{T} \mathcal{K}^O G \\ \frac{S}{L} \mathcal{T}^\dagger \mathcal{K}^M (\mathcal{C}_m E - \mathcal{S}_m D) &= \mathcal{K}^O G \end{aligned} \quad (\text{S14})$$

(v) Between the oxide and the substrate:

$$\begin{aligned} \mathcal{C}_o F - \mathcal{S}_o G &= H \\ \mathcal{K}^O (\mathcal{C}_o G - \mathcal{S}_o F) &= \mathcal{K}^S H \end{aligned} \quad (\text{S15})$$

From Eq. (S15), we can eliminate H to obtain

$$G = (\mathcal{K}^O \mathcal{C}_o + \mathcal{K}^S \mathcal{S}_o)^{-1} (\mathcal{K}^O \mathcal{S}_o + \mathcal{K}^S \mathcal{C}_o) F. \quad (\text{S16})$$

Then, from Eq. (S14) and Eq. (S16), we can eliminate F and G to obtain:

$$E = (\mathcal{V} \mathcal{K}^M \mathcal{C}_m + \mathcal{S}_m)^{-1} (\mathcal{V} \mathcal{K}^M \mathcal{S}_m + \mathcal{C}_m) D, \quad (\text{S17})$$

where $\mathcal{V} = \frac{S}{L} \mathcal{T} (\mathcal{K}^O \mathcal{S}_o + \mathcal{K}^S \mathcal{C}_o)^{-1} (\mathcal{K}^O \mathcal{C}_o + \mathcal{K}^S \mathcal{S}_o) \mathcal{K}^{O-1} \mathcal{T}^\dagger$. Further, from Eq. (S13) and Eq. (S17), we can eliminate D and E to obtain:

$$C = (\mathcal{W} \mathcal{C}_b + \mathcal{K}^B \mathcal{S}_b)^{-1} (\mathcal{W} \mathcal{S}_b + \mathcal{K}^B \mathcal{C}_b) B = \left[\mathcal{K}^{B-1} \mathcal{S}_b \mathcal{C}_b^{-1} + (\mathcal{C}_b \mathcal{W} \mathcal{C}_b + \mathcal{K}^B \mathcal{C}_b \mathcal{S}_b)^{-1} \right] \mathcal{K}^B B, \quad (\text{S18})$$

where $\mathcal{W} = \frac{S}{L} \mathcal{T}^\dagger \mathcal{K}^M (\mathcal{V} \mathcal{K}^M \mathcal{C}_m + \mathcal{S}_m)^{-1} (\mathcal{V} \mathcal{K}^M \mathcal{S}_m + \mathcal{C}_m) \mathcal{T}$ or, equivalently, $\mathcal{W} = \frac{S}{L} \mathcal{T}^\dagger \left[\mathcal{K}^M \mathcal{S}_m \mathcal{C}_m^{-1} + (\mathcal{C}_b \mathcal{V} \mathcal{C}_b + \mathcal{K}^{M-1} \mathcal{C}_m \mathcal{S}_m)^{-1} \right] \mathcal{T}$ (the latter form makes it clear that \mathcal{W} is a Hermitian matrix). From Eq. (S11), we can eliminate R to obtain:

$$A = 2\mathcal{K}^A (\mathcal{K}^A \mathcal{C}_t + \mathcal{K}^B \mathcal{S}_t)^{-1} I - \left[\mathcal{K}^{B-1} \mathcal{S}_t \mathcal{C}_t^{-1} + (\mathcal{C}_t \mathcal{K}^A \mathcal{C}_t + \mathcal{K}^B \mathcal{C}_t \mathcal{S}_t)^{-1} \right] \mathcal{K}^B B, \quad (\text{S19})$$

or we can eliminate A to obtain:

$$R = (\mathcal{K}^A \mathcal{C}_t + \mathcal{K}^B \mathcal{S}_t)^{-1} [(\mathcal{K}^A \mathcal{C}_t - \mathcal{K}^B \mathcal{S}_t) I - \mathcal{K}^B B]. \quad (\text{S20})$$

If there is no external drive input $I = 0$, Eq. (S18), and Eq. (S19) altogether gives:

$$\begin{aligned} C - A &= \mathcal{Y} \mathcal{K}^B B, \text{ where} \\ \mathcal{Y} &= \left[\mathcal{K}^{B-1} \mathcal{S}_t \mathcal{C}_t^{-1} + (\mathcal{C}_t \mathcal{K}^A \mathcal{C}_t + \mathcal{K}^B \mathcal{C}_t \mathcal{S}_t)^{-1} \right] + \left[\mathcal{K}^{B-1} \mathcal{S}_b \mathcal{C}_b^{-1} + (\mathcal{C}_b \mathcal{W} \mathcal{C}_b + \mathcal{K}^B \mathcal{C}_b \mathcal{S}_b)^{-1} \right]. \end{aligned} \quad (\text{S21})$$

Then, by examining Eq. (S10) and recalling the definition of the dynamic capacitance $\delta U_E(\mathbf{q}) = e^2 \sum_{\mathbf{q}'} C^{-1}(\mathbf{q}, \mathbf{q}') \delta n(\mathbf{q}')$, we arrive at

$$C^{-1}(q_m, q_{m'}) = \frac{[\mathcal{Y}^{-1}]_{mm'}}{q_m q_{m'}} = [\mathcal{Q}^{-1} \mathcal{Y}^{-1} \mathcal{Q}^{-1}]_{mm'}. \quad (\text{S22})$$

The inverse of dynamic capacitance is equal to the dynamic coulomb interaction [1–3]. It is easily checked that, in a suspended graphene in vacuum ($h_t, h_b \rightarrow \infty$, $\epsilon_{xy}^B = \epsilon_z^B = \epsilon_0$), the above expression reduces to the expression obtained by taking the 2D Fourier transform of Coulomb potential $e^2 C^{-1}(q_m, q_{m'}) \rightarrow \delta_{mm'} \frac{e^2}{2\epsilon_0 |q_m|}$. Thus, the dynamical dielectric function given in the main text is reduced as a compact matrix form:

$$\epsilon(\mathbf{q}, \omega) = \mathbf{1} - \frac{1}{\omega} \mathcal{Q}^{-1} \mathcal{Y}^{-1} \Sigma \mathcal{Q} = \mathcal{Q}^{-1} \left[\mathbf{1} - \frac{1}{\omega} \mathcal{Y}^{-1} \Sigma \right] \mathcal{Q}. \quad (\text{S23})$$

Therefore, the density of state, which is approximated as the imaginary part of the inverse of the dynamical dielectric function, is given as

$$DOS(\mathbf{q}, \omega) = -\text{Im} [\text{Tr} ([\epsilon(\mathbf{q}, \omega)]^{-1})] = -\text{Im} \left[\text{Tr} \left(\left[\mathbf{1} - \frac{1}{\omega} \mathcal{Y}^{-1} \Sigma \right]^{-1} \right) \right]. \quad (\text{S24})$$

This is the quantity plotted in the main text for the figure containing the HIPP dispersions.

Now, we can combine Eq. (S12), Eq. (S18), and Eq. (S19) to obtain:

$$R = (\mathcal{K}^A \mathcal{C}_t + \mathcal{K}^B \mathcal{S}_t)^{-1} \left[(\mathcal{K}^A \mathcal{C}_t - \mathcal{K}^B \mathcal{S}_t) - 2 \left(\mathcal{Y} - \frac{1}{\omega} \Sigma \right)^{-1} \mathcal{K}^A (\mathcal{K}^A \mathcal{C}_t + \mathcal{K}^B \mathcal{S}_t)^{-1} \right] I. \quad (\text{S25})$$

As mentioned earlier, the reflection upon normal incidence is calculated as $|R_0|^2$ with $I_m = \delta_{m0}$ and $q = 0$.

III. HIPP DISPERSIONS UNDER A DIFFERENT SUPERLATTICE DESIGN

In this section, we show that the appearance of the hybrid intersubband-plasmon-polaritons (HIPPs) shown in the main text is not contingent upon a specific set of parameter conditions, by providing the HIPP dispersions for a

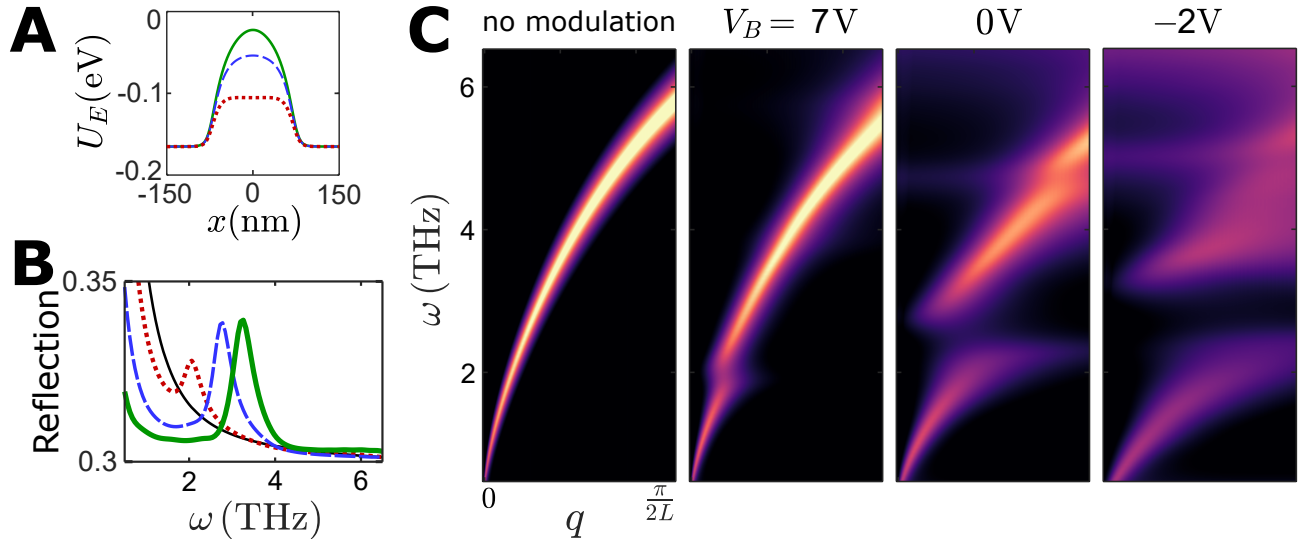


FIG. S2. **a** SL potential $U_E(x)$ (bottom) for different backgate voltages ($V_M = 1V$ is for all three cases); dotted red: $V_B = 7V$, dashed blue: $0V$, and solid green: $-2V$. ($h_t = 5\text{nm}$, $h_b = 10\text{nm}$, $h_g = 10\text{nm}$, $h_0 = 150\text{nm}$, $L = 300\text{nm}$, $S = 150\text{nm}$). **b** Reflection spectra for the normal incidence of light polarized along x -axis; solid thin black: no modulation ($E_F = 0.15\text{eV}$), dotted red: $V_B = 7V$, dashed blue: $0V$, and solid thick green: $-2V$. **c** Density of states or $-\text{Im} [\text{Tr} ([\epsilon(\mathbf{q}, \omega)]^{-1})]$ for visualizing the HIPP dispersion.

different superlattice design. In the main text, the results were shown for a system with a periodicity of $L = 300\text{nm}$ and the air gap width of $S = 80\text{nm}$. Here, in Fig. S2, we provided the same calculations for $S = 150\text{nm}$. For a similar degree of U_E modulation, the intersubband transition (ISBT) frequencies are slightly blue-shifted, compared to the results in the main text, since the potential well width $L - S$ is now deceased. Other than such small details, the HIPP phenomenon is qualitatively the same. Therefore, the experimental verification of this HIPP emergence under 1D SL in graphene would be universally possible for nearly any choice of parameter conditions.

IV. HIPP DISPERSIONS WITH MASSIVE 2D ELECTRON GAS SYSTEMS

In this section, we show that HIPPs and ladder-like equispaced energy bands appear in massive electron systems as well as in a massless Dirac particle system. This might sound intuitively odd, as the energy levels in a square potential well of width W are given as $E_j = \frac{\pi^2 \hbar^2}{2mW^2} j^2$ (m is the effective mass of the electrons). But, this quadratic scaling of energy levels is valid only when the square well is infinitely deep. Since the considered potential wells have finite depths, the energy levels near the Fermi surface appear to be nearly equi-spaced at a high enough k_y (momentum perpendicular to the SL modulation direction). An analysis similar to the one given in the section I can be done for a massive particle, and the bound state formation condition is given as

$$\tan(qW) = \frac{q\alpha}{\frac{m}{\hbar^2}(2E - U_0 - U_1) - k_y^2}, \quad (\text{S26})$$

where $q = \sqrt{\frac{2m}{\hbar^2}(E - U_0) - k_y^2}$ and $\alpha = \sqrt{k_y^2 - \frac{2m}{\hbar^2}(E - U_1)}$ (valid only when $U_0 + \frac{\hbar^2}{2m}k_y^2 < E < U_1 + \frac{\hbar^2}{2m}k_y^2$). Since the inverse tangent of the right hand side is a slowly-varying decreasing function in E at a given k_y (it only decreases smoothly from π to 0 as E increases from $U_0 + \frac{\hbar^2}{2m}k_y^2$ to $U_1 + \frac{\hbar^2}{2m}k_y^2$), the solution to the above equation can be approximately given as $E_j = \frac{\hbar^2}{2m}[\frac{\pi^2}{W^2}(j + \phi_j)^2 + k_y^2] + U_0$, where ϕ_j (the inverse tangent of the right-hand-side of Eq. (S26) normalized by π) is smoothly decreasing from 1 to 0 as j increases. As considered in the main text, if U_0 is a deep enough negative potential, the energy levels around the Fermi surface ($\mu_0 = 0$ was assumed) will have a sufficiently high indices $j \sim j_0 \gg 1$. Then, these energy level spacings can be linearized as follows: $E_{j+1} - E_j \sim \frac{\pi^2 \hbar^2}{mW^2} j_0 (1 + \frac{\delta j}{j_0} + \delta \phi_j)$, where $\delta j = j - j_0 \ll j_0$ and $\delta \phi_j = \phi_{j+1} - \phi_j$. In fact, $\delta \phi_j$ is a slightly increasing function in j when $U_0 < E_j - \frac{\hbar^2}{2m}k_y^2 < \frac{U_0 + U_1}{2}$, and a slightly decreasing function when $\frac{U_0 + U_1}{2} < E_j - \frac{\hbar^2}{2m}k_y^2 < U_1$.

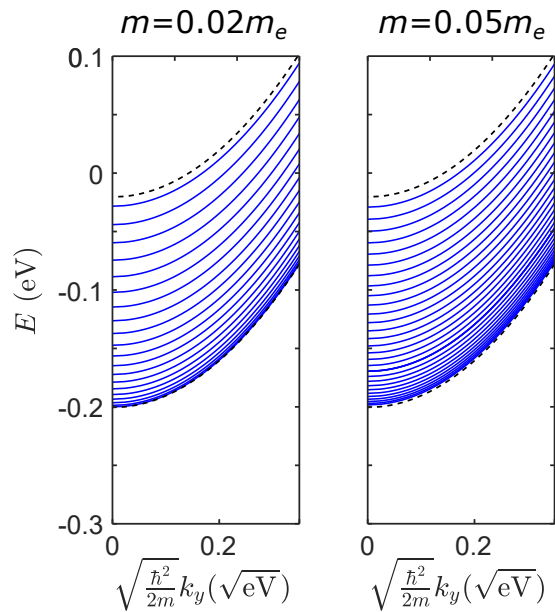


FIG. S3. Bound state solutions to Eq. (S26) for different effective masses (left: $m = 0.02m_e$, right: $m = 0.05m_e$); the square potential well is given as $U_0 = -0.2\text{eV}$ inside the well, $U_1 = -0.02\text{eV}$ outside the well, and the width of the well is 200nm (the same condition considered in Fig. S1). The dashed lines correspond to $E = U_{0,1} + \frac{\hbar^2}{2m}k_y^2$.

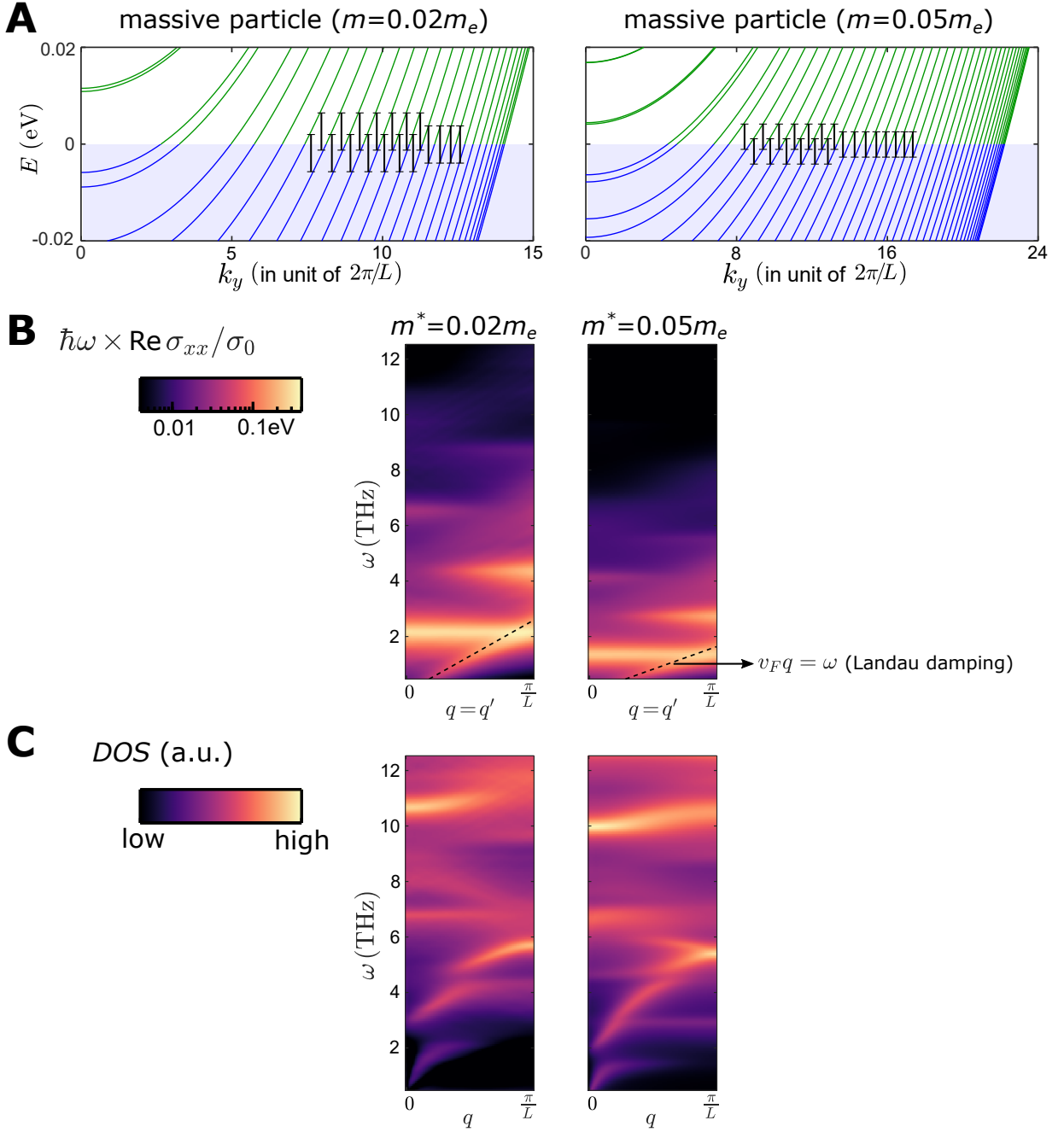


FIG. S4. **a** The electronic subband structure is calculated along k_y at a fixed $k_x = 0$; the SL potential was assumed to be the same as in Fig. 3 in the main text. Each vertical black bar is given as a guide to eyes for denoting a vertical transition ($\Delta j = 1$) from an occupied state below the Fermi surface to a state above the Fermi surface, and all bars have the same length. **b** Real part of the conductivity $\text{Re}[\sigma_{xx}(\mathbf{q} = q\hat{\mathbf{x}}, \mathbf{q}' = q'\hat{\mathbf{x}}; \omega)]$ calculated for $q = q'$; in order to visualize the features at higher frequencies better, we plotted $\omega \times \sigma_{xx}$. **c** Density of states or $-\text{Im}[\text{Tr}[(\epsilon(\mathbf{q}, \omega))^{-1}]]$ for visualizing the HIPP dispersion.

Therefore, the energy spacing can remain nearly constant when $\frac{U_0+U_1}{2} < E_j - \frac{\hbar^2}{2m}k_y^2 < U_1$ (thus, k_y should not be too high), as the change in $\frac{\delta j}{j_0}$ (increases as j increases) gets cancelled by the change in $\delta\phi_j$ (decreases as j increases). Figure S3 clearly shows that the energy level spacing becomes constant at around $E = 0$ and at not too high k_y when $U_0 < 0$ and $|U_0/U_1| \gg 1$. Here, j_0 will be roughly given as $E_{j_0} \sim 0 = \frac{\hbar^2}{2m}[\frac{\pi^2}{W^2}j_0^2 + k_y^2] + U_0$, therefore $j_0 \sim \sqrt{\frac{2mW^2}{\pi^2\hbar^2}|U_0| - \frac{W^2}{\pi^2}k_y^2}$. Thus, the energy level spacing will roughly scale as $E_{j+1} - E_j \sim \frac{\pi^2\hbar^2}{mW^2}j_0 \propto W^{-1}m^{-1/2}$.

Also, note that the realistic potential wells always come with a non-vertical side walls, which means that the

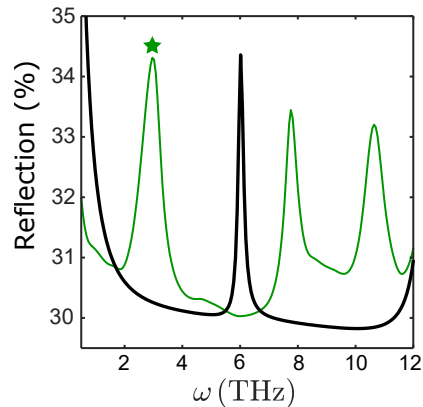


FIG. S5. Reflection spectra shown in Fig. 5 in the main text are replotted with a broader frequency range. Both curves are for $V_B = -9V$ cases; green: exact(kubo) conductivity, black: Drude conductivity.

effective well width slightly increases at higher energies. This factor also helps maintaining the energy level spacing to be nearly constant around the Fermi surface. Figure S4(a) illustrates that the ladder-like equi-spaced energy levels appear in massive particle systems as well. The band structures were obtained by solving the ordinary Schrodinger's equation under the same SL potential used in Fig. 3 in the main text. Then, the optical conductivity was obtained by applying Eq (3) in the main text with the velocity operator $\hat{v}_x = \frac{1}{i} \frac{\hbar}{m} \partial_x$ with the valley degeneracy ignored ($g_\nu = 1$), and the HIPP dispersion was then calculated in the same manner as elaborated above in the section II. The rest of Fig. S4 clearly shows that the HIPP features appear in the massive electron systems. As mentioned in the main text, we needed to set the effective electron mass to be very tiny ($0.02m_e$) to obtain an ISBT frequency similar to the one obtained in the Dirac electron system in graphene. Higher masses would give less ISBT frequencies. Therefore, in order to remain in the reasonable range of the ISBT frequency (at least an order of magnitude greater than the Drude loss γ of the system), the electron mass should be relatively small. For this reason, any TMD monolayers or nitride quantum well systems would not be suitable for this purpose, as the effective electron mass values in those systems around around $0.2 - 0.6m_e$. We suggest gallium arsenide quantum well systems, as the effective electron mass values in InGaAs and GaAs are around $0.04 - 0.07m_e$ [4].

V. COMPARISON (DRUDE VS. EXACT) OF REFLECTION SPECTRA AT HIGHER FREQUENCY

In the main text, Figure 5B and D showed the reflection spectra only for the frequency range (1-5THz) under the first plasmonic bandgap, in order to demonstrate the true emergent nature of HIPP signatures. Here, we provide reflection spectra with a broader frequency range to address a few more observations. In Figure S5, we replotted the reflection spectra for $V_B = -9V$ cases from Figure 5B and D. It is once again clear that the starred peak based on kubo conductivity calculation has no counterpart in the reflection calculated with Drude conductivity, thus suggesting that this HIPP resonance is completely beyond any perturbative effects. Another observation is that the plasmonic resonance from Drude conductivity calculation (around 6THz) shows a similar oscillator strength compared to the starred HIPP resonance. This proves the ultra-strongly coupled nature of our studied HIPPs. The additional peak from exact(kubo) conductivity calculation at 8THz seem to correspond to the plasmonic resonance from Drude calculation. The other peak at 10.5THz is another hybridized response, but it is hard to say if it is a completely emergent peak; as seen in Fig. 5C in the main text, the HIPP dispersions become complex and rich at higher frequencies, making it difficult to understand the band structure in a simple picture (as in local hybridization of an underlying single plasmonic band and a single ISBT resonance).

VI. REFLECTIVITY MODULATION ENGINEERED BY SUBSTRATE PROPERTIES

In the main text, Figure 5D shows the reflection peaks of $\sim 3\%$ with the oxide layer thickness of $h_o = 150\text{nm}$ and the backgate(Si) doping density of $n_{Si,dope} = 10^{15}\text{cm}^{-3}$. Here, we show that this reflectivity resonance feature can be modulated by changing h_o and $n_{Si,dope}$, as these properties would alter the interaction time between the incident/reflected radiation and the emergent HIPP polaritons. Much higher doping density of the silicon backgate makes the backgate more like a metallic mirror, and also introduces more loss to the system). To elaborate more

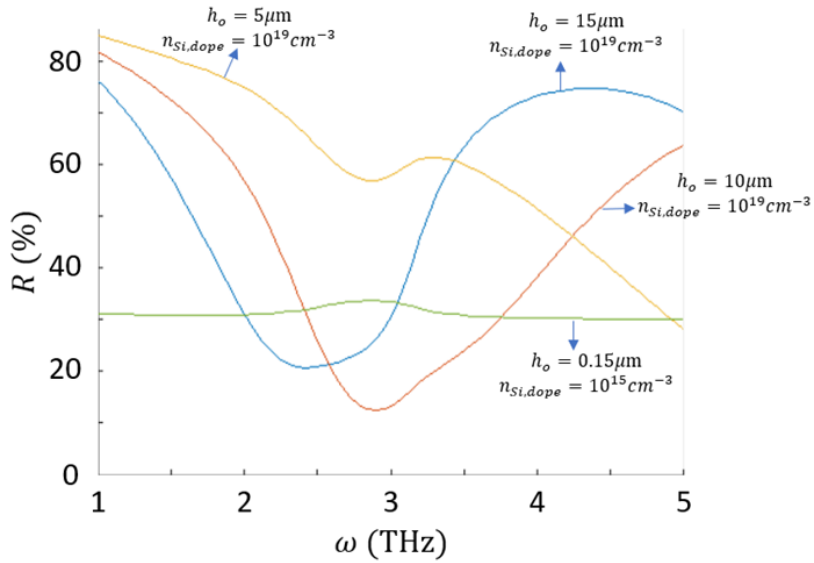


FIG. S6. Reflection spectra shown in Fig. 5 in the main text ($V_B = -9V$ case) are replotted with different choices of substrate conditions h_o and $n_{Si,dope}$.

on the thickness part, since the free space wavelength in this frequency range is $50\mu\text{m}$ (in oxide), increasing SiO₂ thickness upto $25\mu\text{m}$ would enhance the light intensity in the Fabry–Pérot resonator defined between graphene and metallic backgate (but further increase in thickness would introduce Fabry-Pérot resonant peaks in the reflectivity spectrum, which would make the spectra visually more complicated unnecessarily). In Figure S6, we plotted the reflection spectra under different substrate properties (all assuming the same superlattice potential $U_E(x)$ obtained by $V_B = -9V$ and $h_o = 150\text{nm}$ as in Fig. 1 of the main manuscript). Clearly, the resonance can appear in the form of a dip instead of a peak, and also the modulation depth can be up to tens of percents (while sacrificing the sharpness).

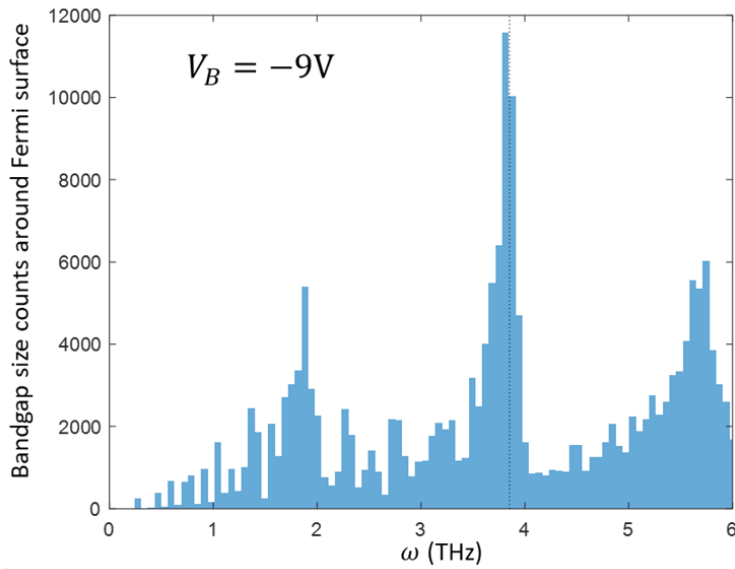


FIG. S7. Bandgap size counts (between filled and empty states) around Fermi surface for $V_B = -9V$ case.

VII. DENSITY OF INTER-STATE ENERGY DIFFERENCES

In the main text, Figure 3 shows the nearly uniform ISBT energy across the fermi surface via band structures. Here, we directly estimate the oscillator strength. In order to get the contribution to the oscillator strengths of optical resonances, we need to look at the density of “inter-state energy differences”, instead of the density of individual state energy levels. When we calculate this density of bandgaps or inter-state energy differences between unoccupied states above the Fermi sea and occupied states below Fermi sea (so that the transitions are possible), we obtained Figure S7. It clearly shows a resonant enhancement at the quantized frequencies (1.9, 3.8, 5.7THz...), agreeing with the resonant peaks shown in the conductivity plots in Fig. 4 in the main manuscript.

-
- [1] M. Jung, Z. Fan, and G. Shvets, [Phys. Rev. Lett. **121**, 086807 \(2018\)](#).
 - [2] I. Torre, M. I. Katsnelson, A. Diaspro, V. Pellegrini, and M. Polini, [Phys. Rev. B **96**, 035433 \(2017\)](#).
 - [3] L. Xiong, C. Forsythe, M. Jung, A. S. McLeod, S. S. Sunku, Y. M. Shao, G. X. Ni, A. J. Sternbach, S. Liu, J. H. Edgar, E. J. Mele, M. M. Fogler, G. Shvets, C. R. Dean, and D. N. Basov, [Nat. Commun. **10**, 4780 \(2019\)](#).
 - [4] V. A. Kulbachinskii, N. A. Yuzeeva, G. B. Galiev, E. A. Klimov, I. S. Vasil’evskii, R. A. Khabibullin, and D. S. Ponomarev, [Semicond. Sci. Technol. **27**, 035021 \(2012\)](#).